

Sol–gel synthesis of porous gadolinium titanate photocatalyst for improved activity

Wenjie Zhang*, Shuyuan Li, Jiaying Zhang, Jiao Yang

School of Environmental and Chemical Engineering, Shenyang Ligong University, Shenyang 110159, China, emails: wjzhang@aliyun.com (W. Zhang), 2874024778@qq.com (S. Li), 3060781822@qq.com (J. Zhang), 1206329565@qq.com (J. Yang)

Received 4 December 2020; Accepted 7 July 2021

ABSTRACT

Polyethylene glycol was used in a sol–gel route to prepare gadolinium titanate. The crystallite sizes of pyrochlore $Gd_2Ti_2O_7$, prepared at 800°C and 900°C were 34.2 and 40.0 nm, respectively. Pores were produced in the materials after removing the PEG1000 template. The bandgap energies of $Gd_2Ti_2O_7$ decreased from 3.43 to 3.21 eV when the calcination temperature increased from 600°C to 900°C. The crystallized porous $Gd_2Ti_2O_7$ had a low photoluminescence intensity. The samples prepared at low calcination temperatures had both a large pore volume and a high specific surface area, and the Brunauer–Emmett–Teller surface area decreased from 46.8 to 14.9 m²/g when the calcination temperature increased from 600°C to 900°C. Hydroxyl radical production and azo dye degradation proved the strongest photocatalytic activity of porous $Gd_2Ti_2O_7$ calcined at 800°C. The Reactive Brilliant Red X-3B degradation efficiency was 43.5% after 30 min of reaction.

Keywords: Gadolinium titanate; Sol-gel; Reactive Brilliant Red X-3B; Photocatalytic degradation; Polyethylene glycol

1. Introduction

Hazardous organic substances make a serious problem to the environment, especially to the aquatic system. The photocatalytic technique was firstly studied on hydrogen evolution from water [1,2]. The most investigated application of the photocatalytic technique was the oxidation of different kinds of hazardous organic substances [3,4]. Most kinds of hazardous organic pollutants were decomposed during the photocatalytic process, and mineralization of organic pollutants was possible [5–7]. For example, the textile industry produces a large amount of wastewater containing azo dyes. Photocatalytic oxidation of azo dyes can lead to the thorough mineralization of complex organic molecules [8].

Photocatalytic efficiency depends on the activity of photocatalysts [9,10]. A novel and active photocatalytic material are always interesting to the development of

photocatalytic techniques. Besides the most applied titania [11–13], some kinds of materials such as AgBr–BaMoO₄ [7], ZnO [14], zinc sulfide [15], CuWO₄ [16], AgIO₄-g-C₃N₄ [17] and titanates [18–20] were reported in the literature. Strontium titanate and barium titanate were the most studied titanates [21,22]. Bisphenol A degradation on La₂Ti₂O₇ was reported by Hua et al. [23]. In our previous work, gadolinium titanate [24,25], lanthanum titanate [26] and cerium titanate [27] were synthesized to remove azo-phloxine and ofloxacin from water.

High-temperature thermal treatment is an important procedure in the preparation of titanate material. However, the as-prepared materials were usually composed of large titanate particles without an apparent porous structure. Photocatalytic activity of large nonporous particles is relatively weak, and the large particles cannot be applied as an acceptable photocatalyst. Templates were used to enhance the porosity of titania [28], and the pores in the materials

* Corresponding author.

usually had positive influences on activity. However, templates were seldom used to prepare titanates until we started a template-mediated sol–gel route to prepare cerium titanate and lanthanum titanate [26,27]. It is important to study the effects of templates on porous titanates. The synthesizing route is also needed to optimize for enhanced activity.

PEG1000 (polyethylene glycol of a molecular weight of 1,000) was used in this work to synthesize gadolinium titanate. This work focused on the synthesizing effects of gadolinium titanate. The materials were characterized, and Reactive Brilliant Red X-3B (RBR X-3B) was used to evaluate the activity of gadolinium titanate. The novelty of this work was to clarify the calcination effects on the porous gadolinium titanate.

2. Materials and methods

2.1. Sol–gel synthesis of porous gadolinium titanate

Porous gadolinium titanate was synthesized by a sol–gel method. All the chemicals were in analytical pure and were obtained from Sinopharm Chemical Reagent Co., Ltd., (China) PEG1000 (1.5 g), tetrabutyl titanate (0.0025 mol) and ethanol (8 mL) were used to prepare solution X. Deionized water (10 mL), acetic acid (8 mL) and $\text{Gd}(\text{NO}_3)_3 \cdot 6\text{H}_2\text{O}$ (0.0025 mol) were used to prepare solution Y. The mixture of solution X and solution Y was stirred to prepare a transparent precursor. The obtained gel was calcined for 3 h at different temperatures to produce gadolinium titanate.

2.2. Characterization of the materials

Crystallization of gadolinium titanate phase in the materials was determined using a D8 X-ray diffractometer (tube voltage 40 kV, $\text{Cu K}\alpha$ $\lambda = 0.15416$ nm). Ultraviolet-visible absorption of the materials was determined using a LAMBDA 35 UV-vis spectrometer. A Quanta 250 scanning electron microscope (SEM) was applied to obtain the surface image. A thin layer of gold was deposited on the samples to avoid charging. High-resolution transmission electron microscopy (HRTEM) image was taken on a transmittance electron microscope (FEI Tecnai G2 20, tube voltage 200 kV). Porosity and Brunauer–Emmett–Teller (BET) surface area was analyzed on a pore analyzer (2460 ASAP). The BET method was used to determine the specific surface area, and the Barrett–Joyner–Halenda method was used to determine the pore size distribution. The photoluminescence spectra emitted by the materials were obtained using a LS-55 fluorescence spectrophotometer.

2.3. Photocatalytic activity measurement

RBR X-3B ($\text{C}_{19}\text{H}_{10}\text{Cl}_2\text{N}_6\text{Na}_2\text{O}_7\text{S}_3$) azo dye was used to determine the activity of gadolinium titanate. 30 mg of gadolinium titanate powders and 50 mL of RBR X-3B solution (30 mg/L) were stirred in the dark until the dye concentration was stable. The adsorption of dye on the materials was calculated after measuring the solution concentration. And then, a 20 W UV lamp was turned on to start the photocatalytic reaction. RBR X-3B degradation efficiency was calculated after the reaction was finished. To determine

hydroxyl radicals on a fluorescence spectrophotometer (PE LS-55), 50 mL of terephthalic acid solution (0.5 mmol/L) was used as the reactant in the same reactor [26]. The terephthalic acid solution was illuminated for 30 min. Total organic carbon (TOC) analysis was conducted using an Analytik Jena multi N/C 3100 TOC/TN analyzer.

3. Results and discussion

3.1. X-ray diffraction analyses of $\text{Gd}_2\text{Ti}_2\text{O}_7$ samples

The X-ray diffraction (XRD) patterns in Fig. 1 were used to determine the phase composition in the materials. As stated in the experimental section, high-temperature calcination was a key factor for the crystallization of gadolinium titanate. There were no apparent diffraction peaks for the samples calcined at 600°C and 700°C, while the diffraction patterns were strong for $\text{Gd}_2\text{Ti}_2\text{O}_7$ samples prepared above 800°C. The diffraction peaks of the gadolinium titanate samples agreed with JCPDS 54-0180, indicating the formation of pyrochlore $\text{Gd}_2\text{Ti}_2\text{O}_7$ crystals in a cubic system. The crystallite sizes of pyrochlore $\text{Gd}_2\text{Ti}_2\text{O}_7$ prepared above 800°C were 34.2 and 40.0 nm, respectively, which were calculated using the Scherrer formula ($L = K\lambda/(\beta\cos\theta)$) [29].

3.2. Surface morphologies of $\text{Gd}_2\text{Ti}_2\text{O}_7$ samples

The morphologies of porous $\text{Gd}_2\text{Ti}_2\text{O}_7$ are presented in Fig. 2. The materials were composed of $\text{Gd}_2\text{Ti}_2\text{O}_7$ particles in the size of several micrometers. The materials tended to aggregate together to form large particles during calcination. As stated before, pyrochlore $\text{Gd}_2\text{Ti}_2\text{O}_7$ crystals were formed above 800°C, and the materials prepared below 700°C did not contain pyrochlore $\text{Gd}_2\text{Ti}_2\text{O}_7$ crystals. However, the particle sizes in all the samples did not have notable differences. PEG1000 was applied to enhance the porosity of $\text{Gd}_2\text{Ti}_2\text{O}_7$. Although PEG1000 molecules could be removed at 600°C [30], the porous structure in the materials prepared below 700°C was not as obvious as the porous

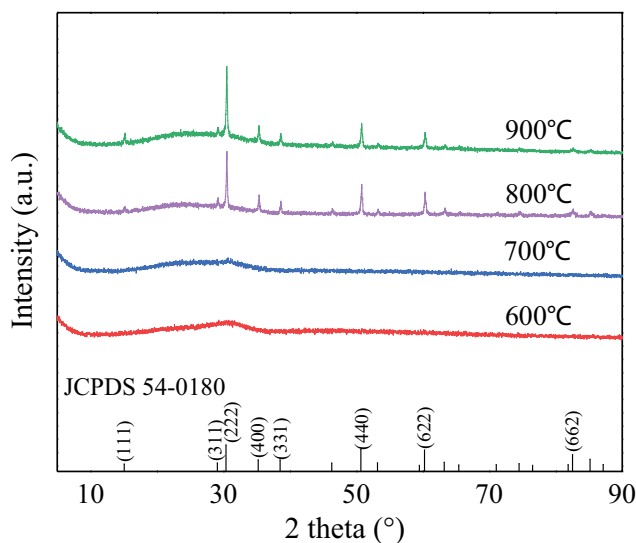


Fig. 1. XRD patterns of $\text{Gd}_2\text{Ti}_2\text{O}_7$ samples.

structure in the materials prepared above 800°C. As presented in Fig. 2c and d, $Gd_2Ti_2O_7$ samples had an apparent porous structure, and the particles were not dense due to the existence of a large number of pores.

Fig. 3 shows the HRTEM image of porous $Gd_2Ti_2O_7$ prepared at 800°C. The high-resolution image of porous $Gd_2Ti_2O_7$ shows a porous structure among $Gd_2Ti_2O_7$ crystals. $Gd_2Ti_2O_7$ crystals were found in the image, and the crystals did not aggregate into large particles. Since hydrolysis and dehydration reactions occurred on PEG1000 molecules, many nucleation centers were formed in the gel to facilitate the crystallization of $Gd_2Ti_2O_7$. The removal of PEG1000 during calcination left pores in porous $Gd_2Ti_2O_7$.

3.3. Fourier-transform infrared spectra of $Gd_2Ti_2O_7$ samples

The chemical bonds in porous $Gd_2Ti_2O_7$ are illustrated in Fig. 4. The absorption around 3429 cm^{-1} is attributed to hydroxyl groups adsorbed on the samples. The absorption peak of the hydroxyl group is quite weak at 1645 cm^{-1} , and the absorption intensity of hydroxyl groups became weaker for the samples calcined at a higher temperature. The absorptions at 447 and 587 cm^{-1} are due to O–Gd–O bond [31]. C–H stretching vibration in saturated

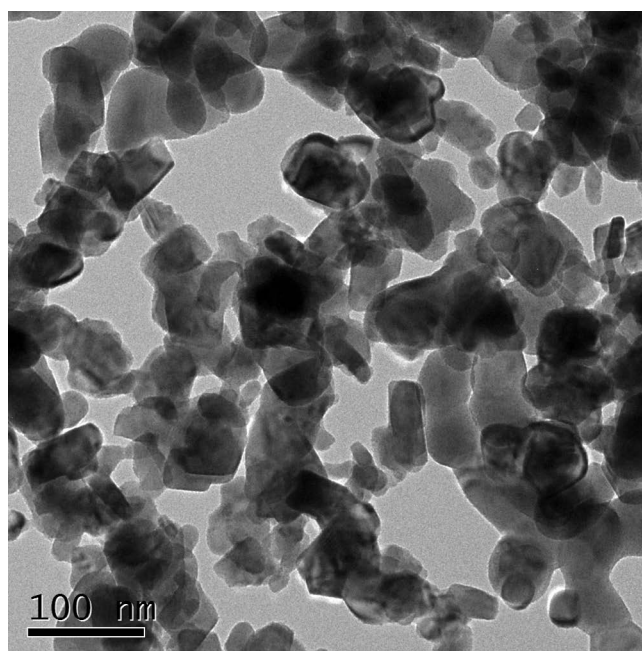


Fig. 3. HRTEM image of porous $Gd_2Ti_2O_7$ prepared at 800°C.

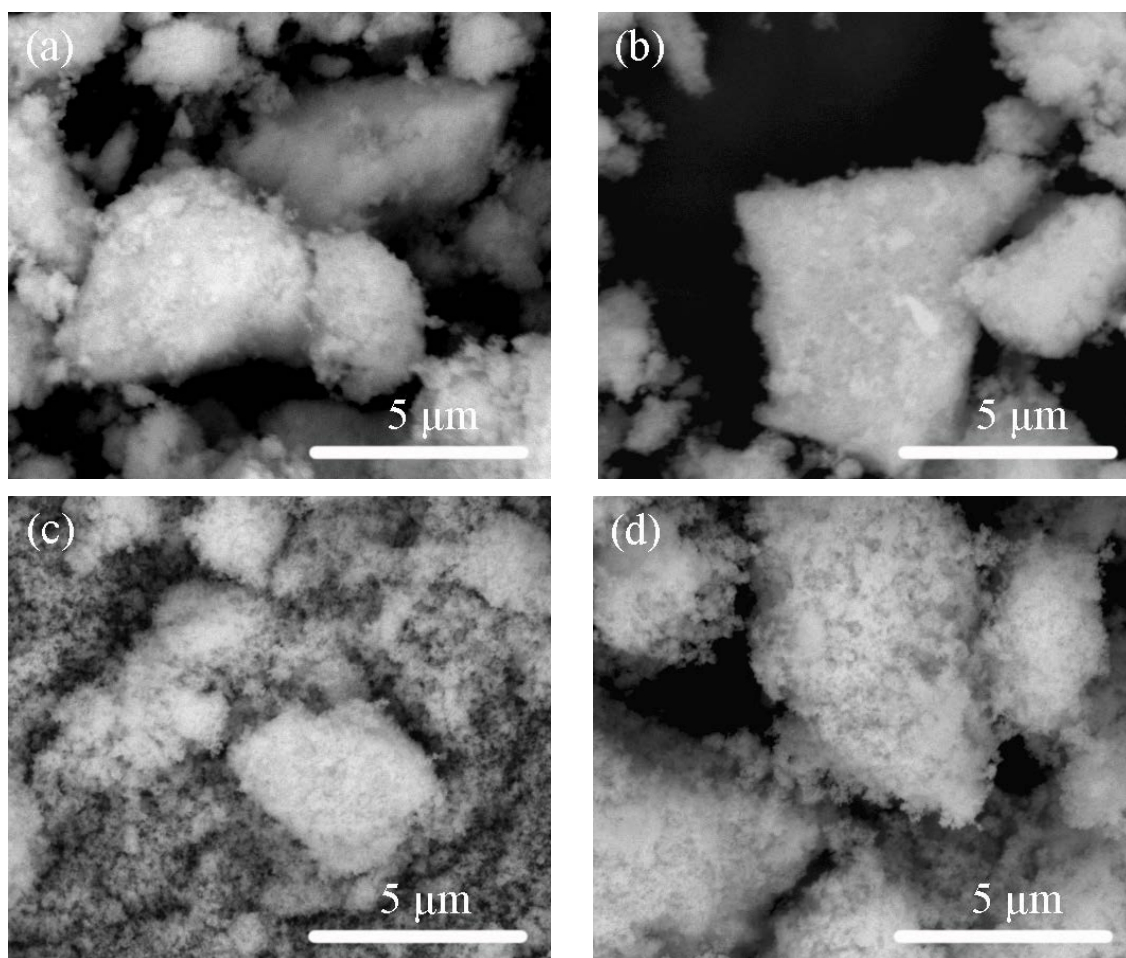


Fig. 2. SEM images of porous $Gd_2Ti_2O_7$ prepared at (a) 600°C, (b) 700°C, (c) 800°C and (d) 900°C.

alkanes is at 2,921 and 2,853 cm^{-1} , and C–H stretching vibration in CH_2 is at 1,515 and 1,387 cm^{-1} . Porous $\text{Gd}_2\text{Ti}_2\text{O}_7$ were mainly composed of gadolinium titanate, and there was still a small amount of organic residue. Meanwhile, the surface adsorbed hydroxyl group is also important because hydroxyl groups can be utilized to generate hydroxyl radicals under irradiation.

3.4. UV-vis diffuse reflectance spectra of $\text{Gd}_2\text{Ti}_2\text{O}_7$ samples

Fig. 5a shows the UV-vis absorption property of $\text{Gd}_2\text{Ti}_2\text{O}_7$ to clarify the influence of calcination on bandgap energy. The absorption edges of porous $\text{Gd}_2\text{Ti}_2\text{O}_7$ were all below 400 nm in the ultraviolet region. Porous $\text{Gd}_2\text{Ti}_2\text{O}_7$ could not respond to visible light, and the materials could absorb the irradiation below a particular ultraviolet

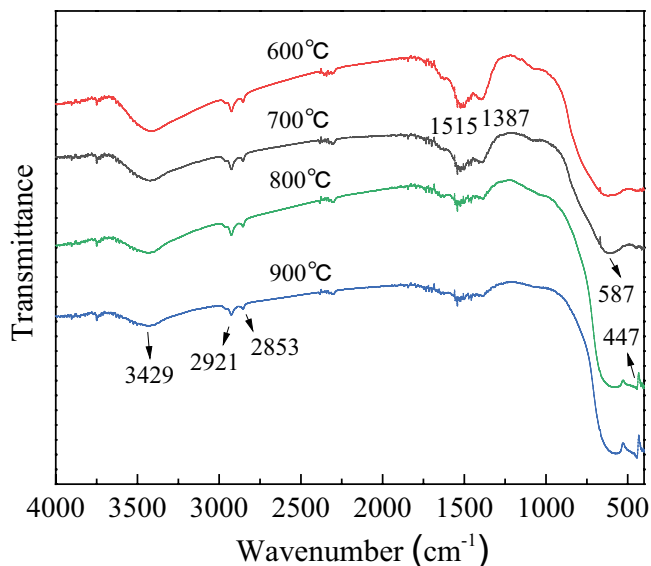
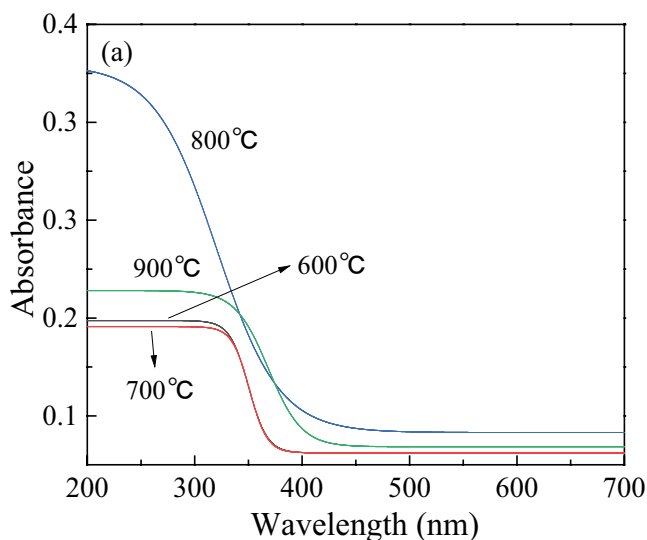


Fig. 4. Fourier-transform infrared spectra of porous $\text{Gd}_2\text{Ti}_2\text{O}_7$.



wavelength. The $h\nu - (\alpha h\nu)^2$ plots of porous $\text{Gd}_2\text{Ti}_2\text{O}_7(n)$ are shown in Fig. 5b. The bandgap energies of $\text{Gd}_2\text{Ti}_2\text{O}_7(n)$ calcined at 600°C, 700°C, 800°C and 900°C were 3.43, 3.42, 3.37 and 3.21 eV, respectively. The increase in calcination temperature led to a slight decrease in bandgap energy. This phenomenon might be attributed to enhanced crystallization of pyrochlore $\text{Gd}_2\text{Ti}_2\text{O}_7$, which was related to the well-known quantum size effect.

3.5. Photoluminescence spectra of $\text{Gd}_2\text{Ti}_2\text{O}_7$ samples

Porous $\text{Gd}_2\text{Ti}_2\text{O}_7$ were examined in a fluorescence spectrophotometer to obtain the photoluminescence spectra. The excitation wavelength was 253.7 nm, and the photoluminescence spectra were recorded in the wavelength region between 400 and 600 nm, as shown in Fig. 6. The electron-hole pairs might recombine together to emit photoluminescence spectra, and therefore, a low intensity in the photoluminescence spectrum means a low frequency in electron-hole recombination. Porous $\text{Gd}_2\text{Ti}_2\text{O}_7$ calcined at 600°C and 700°C had much higher photoluminescence intensities than the photoluminescence intensities of the samples calcined at 800°C and 900°C. The crystallized porous $\text{Gd}_2\text{Ti}_2\text{O}_7$ had a low photoluminescence intensity. Since the lifetimes of charge carriers, that is, electrons and holes, are very important to photocatalytic reaction, reduced recombination of photogenerated charge carriers must be beneficial to the activity of photocatalyst. It can be supposed that the crystallized porous $\text{Gd}_2\text{Ti}_2\text{O}_7$ might have high photocatalytic activity.

3.6. Porosity of $\text{Gd}_2\text{Ti}_2\text{O}_7$ samples

The N_2 adsorption-desorption isotherms of porous $\text{Gd}_2\text{Ti}_2\text{O}_7$ are illustrated in Fig. 7a. The number of N_2 molecules adsorbed on porous $\text{Gd}_2\text{Ti}_2\text{O}_7$ was small when N_2 relative pressure was lower than 0.75. The adsorption capacity of porous $\text{Gd}_2\text{Ti}_2\text{O}_7$ decreased with a rising calcination temperature. The adsorbed N_2 quantity was nearly

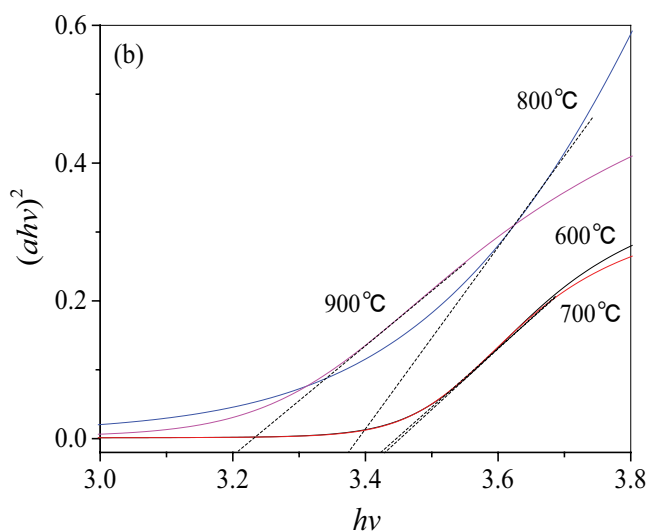


Fig. 5. (a) UV-vis diffuse reflectance spectra of porous $\text{Gd}_2\text{Ti}_2\text{O}_7$, and (b) $h\nu - (\alpha h\nu)^2$ plots.

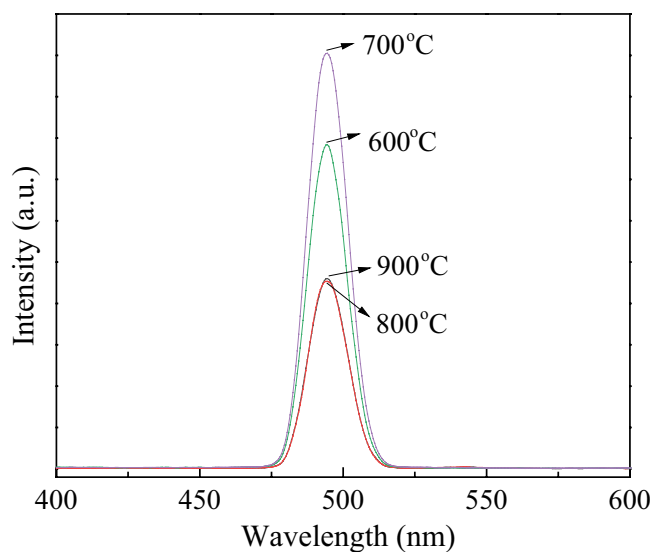


Fig. 6. Photoluminescence spectra of porous $Gd_2Ti_2O_7$ after excitation at 253.7 nm.

unchanged in the wide P/P_0 range below 0.7. On the other hand, the adsorbed N_2 quantity increased quickly when P/P_0 was higher than 0.9, which could be attributed to gaseous N_2 condensation in the small pores of porous $Gd_2Ti_2O_7$.

The above-mentioned isotherms of porous $Gd_2Ti_2O_7$ were a typical IUPAC type IV isotherm, which was used to clarify porous characteristics of mesoporous material. The hysteric loop in IUPAC type IV isotherm is also a key characteristic of mesoporous material. The adsorption hysteresis and desorption hysteresis resulted in the separation of the adsorption and the desorption isotherms. Fig. 7b illustrates pore size distributions of porous $Gd_2Ti_2O_7$. The pore volume was apparently reduced with a rising calcination temperature.

Table 1 lists the pore volume and the BET surface area of porous $Gd_2Ti_2O_7$. The pore volume and the surface area of porous $Gd_2Ti_2O_7$ apparently declined with a rising calcination temperature. The samples prepared at lower calcination temperature had both a larger pore volume and a higher specific surface area. PEG1000 template was used to promote the porosity of the materials, and PEG1000 molecules were likely removed during the calcination process. Calcination temperature could influence the removal of the PEG1000 template, and the organic residues might provide many pores.

The formation of pyrochlore $Gd_2Ti_2O_7$ crystals depended on calcination temperature too. The growth of $Gd_2Ti_2O_7$ crystals at a higher temperature also caused the formation

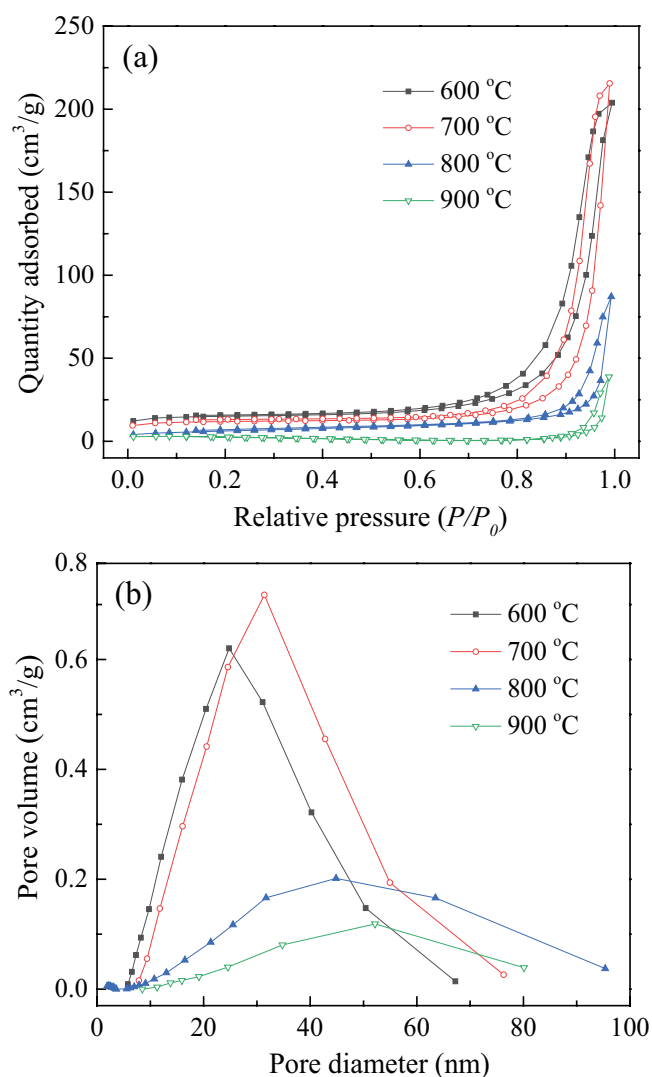


Fig. 7. (a) N_2 adsorption–desorption isotherms and (b) pore size distributions of porous $Gd_2Ti_2O_7$.

of large pores. The amorphous samples calcined below $700^\circ C$ contained many micropores to provide the majority surface area. Meanwhile, the large pore volumes were due to the mesopores, since the micropores could not have a large pore volume. Accompanied by the removal of organic residues at higher calcination temperature and growth of $Gd_2Ti_2O_7$ crystals, the micropores in the materials were emerged into large pores. However, the number of large pores in the samples calcined above $800^\circ C$ were

Table 1
Surface areas and pore volumes of porous $Gd_2Ti_2O_7$.

Calcination temperature ($^\circ C$)	BET surface area (m^2/g)	Micropore surface area (m^2/g)	Pore volume (cm^3/g)
600	46.8	34.61	0.0230
700	36.9	27.28	0.0181
800	21.6	2.93	0.0090
900	14.9	1.35	0.0062

small, which was in accordance with a small pore volume. The sample calcined at 900°C had a very small micropore surface area, so the sample contained a very small number of micropores.

3.7. Hydroxyl radical production on porous $Gd_2Ti_2O_7$

Hydroxyl radicals were generated in the photocatalytic process after the material absorbed photons with enough energy. Monitor of hydroxyl radicals could clarify the activity of materials in a quantitative method. 2-hydroxy-terephthalic acid was a product of terephthalic acid in photocatalytic reaction. The number of 2-hydroxy-terephthalic acid was used to identify the number of hydroxyl radicals. Fig. 8 shows the fluorescence intensity of the solution in the presence of porous $Gd_2Ti_2O_7$. The higher the fluorescence intensity of the solution, the larger number of hydroxyl radicals produced during the photocatalytic process. Obviously, if sufficient hydroxyl radicals were produced in the reaction, the photocatalyst must have strong activity. Since the maximum hydroxyl radicals were produced in the presence of porous $Gd_2Ti_2O_7$ calcined at 800°C, the sample might have the strongest photocatalytic activity.

3.8. Photocatalytic degradation of RBR X-3B

Fig. 9 shows the dye removal efficiencies on porous $Gd_2Ti_2O_7$. Adsorption of the dye was determined when the adsorption rate was as the same as the desorption rate, that is, the adsorption–desorption equilibrium. As stated before, $Gd_2Ti_2O_7$ calcined at low temperature contained some organic residues. The amorphous samples calcined below 700°C contained many micropores that provided the majority of surface area. This could be the reason for the large adsorption capacity. The samples calcined above 800°C had a very small number of micropores, so the adsorption efficiencies became low.

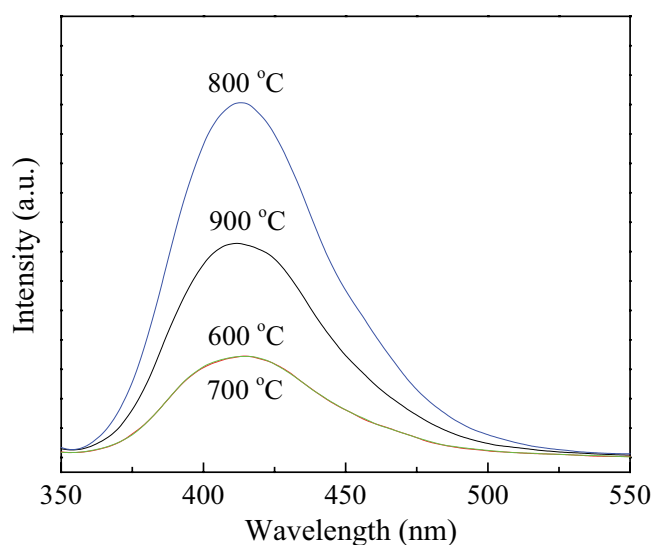


Fig. 8. Fluorescence spectra of 2-hydroxyterephthalic acid solution after 30 min UV illumination in the presence of porous $Gd_2Ti_2O_7$.

The photocatalytic activity was much more concerned than adsorption capacity of the materials. The amorphous $Gd_2Ti_2O_7$ calcined below 700°C had a very poor photocatalytic activity on dye decomposition, while less than 9% of azo dye molecules were decomposed in 30 min. Meanwhile, the degradation efficiency could be as large as 43.5% for the sample calcined at 800°C. However, the degradation efficiency slightly decreased with a further rising calcination temperature. The porous $Gd_2Ti_2O_7$ obtained at 800°C seemed to be the optimal material because it had strong photocatalytic activity and a not very large adsorption capacity. The key role of a photocatalyst is the activity on organic substances degradation.

The organic carbon removal efficiency was determined in the presence of $Gd_2Ti_2O_7$ prepared at 800°C. Although the organic carbon concentration in the dye solution was reduced in the photocatalytic reaction, the TOC removal efficiency was not as high as the dye decoloration efficiency. RBR X-3B solution was completely decolorized in 100 min. However, only 16.7% of the TOC in the solution was removed in 120 min.

The mass of porous $Gd_2Ti_2O_7$ prepared at 800°C could also affect RBR X-3B degradation efficiency. The degradation efficiency increased from 22.8% (10 mg $Gd_2Ti_2O_7$) to 52.0% (50 mg $Gd_2Ti_2O_7$). However, the increase in degradation efficiency with a rising photocatalyst mass became slow after using high $Gd_2Ti_2O_7$ mass. 30 mg of $Gd_2Ti_2O_7$ was used in all the reactions.

Fig. 10 shows the pH effect of RBR X-3B solution on the adsorption and degradation of RBR X-3B in the presence of porous $Gd_2Ti_2O_7$ prepared at 800°C. The initial RBR X-3B solution (30 mg/L) had a pH of 5.24. The pH of the solution was adjusted by adding hydrochloric acid solution (0.3 mol/L) or NaOH solution (0.3 mol/L). RBR X-3B degradation efficiency constantly decreased with a rising pH of the solution.

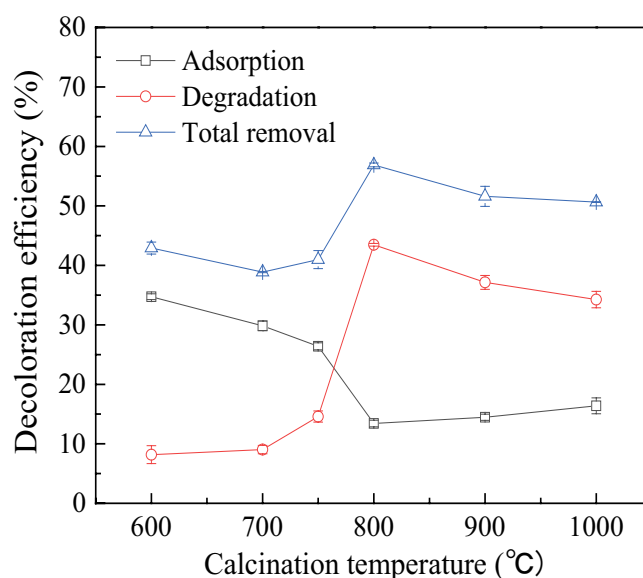


Fig. 9. Adsorption and photocatalytic degradation of RBR X-3B on porous $Gd_2Ti_2O_7$. The illumination time was 30 min for the reaction.

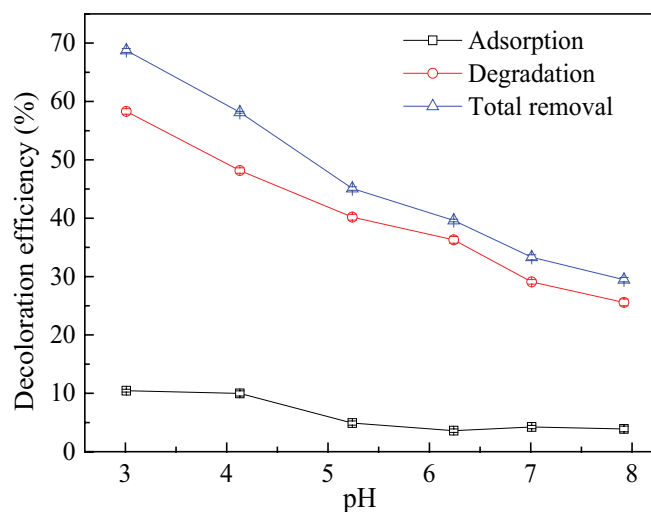


Fig. 10. Adsorption and degradation of RBR X-3B as a function of solution pH in the presence of $Gd_2Ti_2O_7$ prepared at $800^\circ C$. The reaction time was 30 min.

4. Conclusions

Porous $Gd_2Ti_2O_7$ prepared below $700^\circ C$ was in the amorphous phase, while pyrochlore $Gd_2Ti_2O_7$ crystals formed above $800^\circ C$. $Gd_2Ti_2O_7$ materials obtained at high temperature became porous after removing the template. The increase in calcination temperature led to a slight decrease in the bandgap energy. The pore volume and the surface area of the materials apparently declined with a rising calcination temperature. The maximum hydroxyl radicals were generated in the presence of porous $Gd_2Ti_2O_7$ prepared at $800^\circ C$, which also had the strongest photocatalytic activity on azo dye degradation.

References

- [1] A. Fujishima, K. Honda, Electrochemical photolysis of water at a semiconductor electrode, *Nature*, 238 (1972) 37–38.
- [2] M.A. Ahmed, A. Fahmy, M.G. Abuzaid, E.M. Hashem, Fabrication of novel $AgIO_3/SnO_2$ heterojunction for photocatalytic hydrogen production through direct Z-scheme mechanism, *J. Photochem. Photobiol., A*, 400 (2020) 112660, doi: 10.1016/j.jphotochem.2020.112660.
- [3] Z. Zhu, P. Huo, Z. Lu, Y. Yan, Z. Liu, W. Shi, C. Li, H. Dong, Fabrication of magnetically recoverable photocatalysts using $g-C_3N_4$ for effective separation of charge carriers through like-Z-scheme mechanism with Fe_3O_4 mediator, *Chem. Eng. J.*, 331 (2018) 615–625.
- [4] M.R. Hoffmann, S.T. Martin, W. Choi, W. Bahnemann, Environmental applications of semiconductor photocatalysis, *Chem. Rev.*, 95 (1995) 69–96.
- [5] A. Koltsakidou, Ch. Katsiloulis, E. Evgenidou, D.A. Lambropoulou, Photolysis and photocatalysis of the non-steroidal anti-inflammatory drug Nimesulide under simulated solar irradiation: kinetic studies, transformation products and toxicity assessment, *Sci. Total Environ.*, 689 (2019) 245–257.
- [6] Z. Li, M. Qi, C. Tu, W. Wang, J. Chen, A.J. Wang, Highly efficient removal of chlorotetracycline from aqueous solution using graphene oxide/ TiO_2 composite: Properties and mechanism, *Appl. Surf. Sci.*, 425 (2017) 765–775.
- [7] S.K. Ray, D. Dhakal, S.W. Lee, Insight into sulfamethoxazole degradation, mechanism, and pathways by $AgBr-BaMoO_4$ composite photocatalyst, *J. Photochem. Photobiol., A*, 364 (2018) 686–695.
- [8] J. Ambigadevi, P.S. Kumar, D.-V.N. Vo, S.H. Haran, T.N.S. Raghavan, Recent developments in photocatalytic remediation of textile effluent using semiconductor based nanostructured catalyst: a review, *J. Environ. Chem. Eng.*, 9 (2021) 104881, doi: 10.1016/j.jece.2020.104881.
- [9] S. Cen, X.G. Lv, Y. Jiang, A. Fakhri, V.K. Gupta, Synthesis and structure of iron-copper/hollow magnetic/metal-organic framework/coordination sites in a heterogeneous catalyst for a Fenton-based reaction, *Catal. Sci. Technol.*, 10 (2020) 6687–6693.
- [10] M.A. Ashraf, C. Li, D. Zhang, L. Zhao, A. Fakhri, Fabrication of silver phosphate-ilmenite nanocomposites supported on glycol chitosan for visible light-driven degradation, and antimicrobial activities, *Int. J. Biol. Macromol.*, 169 (2021) 436–442.
- [11] Y. Ku, S.J. Shiu, H.C. Wu, Decomposition of dimethyl phthalate in aqueous solution by UV-LED/ TiO_2 process under periodic illumination, *J. Photochem. Photobiol., A*, 332 (2017) 299–305.
- [12] M. Bellardita, A. Paola, B. Megna, L. Palmisano, Absolute crystallinity and photocatalytic activity of brookite TiO_2 samples, *Appl. Catal., B*, 201 (2017) 150–158.
- [13] H.S.M. Abd-Rabboh, M. Benaissa, M.S. Hamdy, M.A. Ahmed, M. Glal, Synthesis of an efficient, and recyclable mesoporous $BiVO_4/TiO_2$ direct Z-scheme heterojunction by sonochemical route for photocatalytic hydrogen production and photodegradation of rhodamine B dye in the visible region, *Opt. Mater.*, 114 (2021) 110761, doi: 10.1016/j.optmat.2020.110761.
- [14] I.J. Ani, U.G. Akpan, M.A. Olutoye, B.H. Hameed, Photocatalytic degradation of pollutants in petroleum refinery wastewater by TiO_2 - and ZnO-based photocatalysts: recent development, *J. Cleaner Prod.*, 205 (2018) 930–954.
- [15] A. Mehrizad, M.A. Behnajady, P. Gharbani, S. Sabbagh, Sonocatalytic degradation of Acid Red 1 by sonochemically synthesized zinc sulfide-titanium dioxide nanotubes: optimization, kinetics and thermodynamics studies, *J. Cleaner Prod.*, 215 (2019) 1341–1350.
- [16] Y. Cai, F. Yang, L. Wu, Y. Shu, G. Qu, A. Fakhri, V.K. Gupta, Hydrothermal-ultrasonic synthesis of CuO nanorods and $CuWO_4$ nanoparticles for catalytic reduction, photocatalysis activity, and antibacterial properties, *Mater. Chem. Phys.*, 258 (2021) 123919, doi: 10.1016/j.matchemphys.2020.123919.
- [17] N. Al-Zaqri, A. Alsalmeh, M.A. Ahmed, A.H. Galal, Construction of novel direct Z-scheme $AgIO_3-g-C_3N_4$ heterojunction for photocatalytic hydrogen production and photodegradation of fluorescein dye, *Diamond Relat. Mater.*, 109 (2020) 108071, doi: 10.1016/j.diamond.2020.108071.
- [18] L.M. Lozano-Sánchez, S. Obregón, L.A. Díaz-Torres, S. Lee, V. Rodríguez-González, Visible and near-infrared light-driven photocatalytic activity of erbium-doped $CaTiO_3$ system, *J. Mol. Catal., A*, 410 (2015) 19–25.
- [19] Z. Chen, H. Jiang, W. Jin, C. Shi, Enhanced photocatalytic performance over $Bi_4Ti_3O_{12}$ nanosheets with controllable size and exposed {001} facets for Rhodamine B degradation, *Appl. Catal., B*, 180 (2016) 698–706.
- [20] Y.A. Zulueta, M.T. Nguyen, Multisite occupation of divalent dopants in barium and strontium titanates, *J. Phys. Chem. Solids*, 121 (2018) 151–156.
- [21] B. Kiss, T.D. Manning, D. Hesp, C. Didier, M.J. Rosseinsky, Nano-structured rhodium doped $SrTiO_3$ -visible light activated photocatalyst for water decontamination, *Appl. Catal., B*, 206 (2017) 547–555.
- [22] K. Katagiri, Y. Miyoshi, K. Inumaru, Preparation and photocatalytic activity of strontium titanate nanocube-dispersed mesoporous silica, *J. Colloid Interface Sci.*, 407 (2013) 282–286.
- [23] Z.L. Hua, X.Y. Zhang, X. Bai, L.L. Lv, Z.F. Ye, X. Huang, Nitrogen-doped perovskite-type $La_2Ti_2O_7$ decorated on graphene composites exhibiting efficient photocatalytic activity toward Bisphenol A in water, *J. Colloid Interface Sci.*, 450 (2015) 45–53.
- [24] W.J. Zhang, Y.J. Tao, C.G. Li, Sol-gel synthesis and characterization of $Gd_2Ti_2O_7/SiO_2$ photocatalyst for ofloxacin decomposition, *Mater. Res. Bull.*, 105 (2018) 55–62.

- [25] W.J. Zhang, Y.J. Tao, C.G. Li, Sol-gel synthesis of $Gd_2Ti_2O_7$ /HZSM-5 composite photocatalyst for ofloxacin degradation, *J. Photochem. Photobiol., A*, 364 (2018) 787–793.
- [26] W.J. Zhang, H.L. Li, Z. Ma, H. Li, H. Wang, Photocatalytic degradation of azophloxine on porous $La_2Ti_2O_7$ prepared by sol-gel method, *Solid State Sci.*, 87 (2019) 58–63.
- [27] W.J. Zhang, J. Yang, C.G. Li, Role of thermal treatment on sol-gel preparation of porous cerium titanate: characterization and photocatalytic degradation of ofloxacin, *Mater. Sci. Semicond. Process.*, 85 (2018) 33–39.
- [28] Y. Zhang, C. Han, G. Zhang, D. Dionysiou, M. Nadagoudaf, PEG-assisted synthesis of crystal TiO_2 nanowires with high specific surface area for enhanced photocatalytic degradation of atrazine, *Chem. Eng. J.*, 268 (2015) 170–179.
- [29] A. Patterson, The Scherrer formula for X-ray particle size determination, *Phys. Rev.*, 56 (1939) 978–982.
- [30] W.J. Zhang, R.Y. Li, H.B. He, Synthesis of mesoporous TiO_2 - Al_2O_3 binary oxides by sol-gel method using PEG1000 template, *Inf. J. Photoenergy*, 2012 (2012) 108175.
- [31] L. Kong, I. Karatchevtseva, D.J. Gregg, M.G. Blackford, R. Holmes, G. Triani, $Gd_2Zr_2O_7$ and $Nd_2Zr_2O_7$ pyrochlore prepared by aqueous chemical synthesis, *J. Eur. Ceram. Soc.*, 33 (2013) 3273–3285.